ACS OMEGA

Open Access

http://pubs.acs.org/journal/acsodf

Article

Crystal Structure and Spectroscopic Characterization of a New Hybrid Compound, $(C_{12}H_{17}N_2)_2[CdBr_4]$, for Energy Storage Applications

Arafet Ghoudi, Sandy Auguste, Jérome Lhoste, Walid Rekik, Houcine Ghalla, Kamel Khirouni, Abdelhedi Aydi, and Abderrazek Oueslati*

Cite This: *ACS Omega* 2024, 9, 28339−28353

Read Online

ACCESS | Metrics & More | Article Recommendations

ABSTRACT: Organic−inorganic hybrid materials have recently found a vast variety of applications in the fields of energy storage and microelectronics due to their outstanding electric and dielectric characteristics, including high dielectric constant, low conductivity, and low dielectric loss. However, despite the promising properties of these materials, there remains a need to explore novel compounds with improved performance for practical applications. In this research paper, the focus is on addressing this scientific challenge by synthesizing and characterizing the new-centrosymmetric $(C_{12}H_{17}N_2)_2[CdBr_4]$ crystal. This compound offers potential advancements in energy storage technologies and microelectronics due to its unique structural and electronic properties. The chemical mentioned above crystallizes in the monoclinic system, and its protonated amine $(C_{12}H_{17}N_2)^+$ and isolated anion $[CdBr_4]^{2-}$ are bound by C−H···π and N−H···Br hydrogen bonds to form its zero-dimensional structure. Through optical absorption analysis, the semiconductor nature of the material is verified, showcasing a band gap of around 2.9 eV. Furthermore, an in-depth examination of Nyquist plots reveals the material's electrical characteristics' sensitivity to frequency and temperature variations. By applying Jonscher's power law to analyze ac conductivity plots, it is observed that the variation in the exponent "s" accurately characterizes the conduction mechanism, aligning with CBH models. The compound exhibits low dielectric loss values and a high permittivity value ($\varepsilon \sim 10^5$), making it a promising candidate for energy storage applications. By managing the scientific challenge of improving material performance for energy storage and microelectronics, this research contributes to advancing the field and opens avenues for further exploration and application of organic−inorganic hybrid materials.

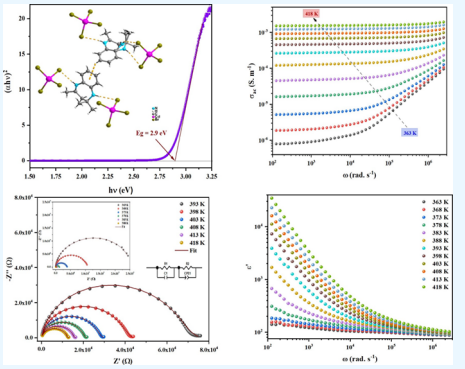

1. INTRODUCTION

The study area is now more focused on organic−inorganic materials, as they have gained significant interest and become an essential component due to their new physicochemical features.[1−5] Aside from being a brand-new area of basic study, they also offer new opportunities for applications in various industries, including solid electrolytes, optics, biomedicine, and catalysis.[6−9] Additionally, they are becoming more significant in energy storage, flash memory technology, and optoelectronics applications such as lasers and smart windows.[10−14] However, optical sensing is one area where metal halide perovskite single crystals excel. They are excellent for converting light signals into electrical ones, acting as high-efficiency photodetectors, because of their high responsivity and specific detectivity.[15,16] Due to their numerous physical and chemical characteristics, such as piezoelectricity, ferroelectricity, luminescence, and photocatalysis, complexes with the chemical formula A_2MX_4 (A = organic cation, M = transition divalent metal ion, X = halide ion) have attracted considerable interest among hybrid materials.[17,18] Particularly, hybrid compounds based on cadmium halide have drawn interest in particular due to the many coordination topologies and structural flexibility of the Cd^{2+} ion.[19,20] During the construction of novel cadmium-based compounds, organic templates are important in establishing their structures and properties. At the same time, the concentration, size, charge density, and crystal packing of cations, as well as the metal's properties, have a considerable impact on the anion component's size and dimensions. In general, N−H···X hydrogen bonds are typically used to bind inorganic parts of organic molecules. As a result, the substitution of organic groups can provide the hybrid material with more stability and

Received: February 29, 2024
Revised: May 2, 2024
Accepted: May 9, 2024
Published: June 20, 2024

https://doi.org/10.1021/acsomega.4c01997
ACS Omega 2024, 9, 28339−28353

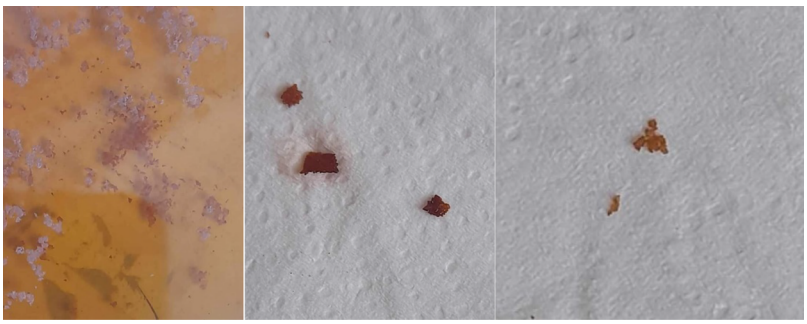

Figure 1. Crystals of the $(C_{12}H_{17}N_2)_2[CdBr_4]$ compound.

more novel features, expanding the range of potential applications of these materials. Researchers have so far effectively created cadmium-based organic−inorganic hybrid materials employing organic groups such as methylamine, cyclohexylamine, alkylammonium, etc.[21,22] However, the stability and optical band gap for optoelectronic devices need to be researched and improved. Therefore, the need for an organic−inorganic hybrid cadmium-based material with a strong band gap and a high band stability is essential. Pyridine and its derivatives are used as organic templates in the creation of organic−inorganic hybrid materials, which have intriguing physical characteristics[23,24] and biological functions.[25] A variety of special benefits, such as high electrical mobility, adjustable band gap, tunable magnetic characteristics, and strong thermal stability, are found only in materials containing halogenated metal pyridine compounds.

As part of our current study, we report our investigations on a new cadmium-based organic−inorganic compound with the general chemical formula of $(C_{12}H_{17}N_2)_2[CdBr_4]$. The structural, optical, and electric characterizations were performed in this work.

2. EXPERIMENTAL DETAILS

2.1. Crystallization of $[C_{12}H_{17}N_2]_2CdBr_4$. The synthesis of the $(C_{12}H_{17}N_2)_2[CdBr_4]$ compound was carried out using a similar preparation procedure of other hybrid compounds that were reported before (Solvent evaporation method).[6,23] The synthesis process begins with the dissolution of 1,2-benzen diammonium in an acetone solution at room temperature to prepare the chemical molecule $C_{12}H_{16}N_2$. The resulting solution containing $C_{12}H_{16}N_2$ is combined with CdBr2 dissolved in HBr in a 2:1 molar ratio. Good-quality white single crystals, as shown in Figure 1, were obtained by slow evaporation of the mixture at room temperature (10 days). The single crystals were washed with absolute ethanol and dried in vacuum desiccators.

2.2. Single-Crystal Diffraction Data Collection and Structure Determination. A suitable single crystal of the title compound ($0.57 \times 0.40 \times 0.30$ mm^3) was chosen under a polarizing microscope and placed on a four-circle BRUKER APEX II area-detector diffractometer. The reflection data were acquired by using graphite-monochromated Kα(Mo) radiation (λ = 0.71073 Å). All Intensity data were collected at 296(2) K through the program APEX 2.[26] An Empirical absorption correction of multiscan type was performed with the program SADABS.[27] The crystal structure was solved in the centrosymmetric space group $P2_1/n$ using the ShelxT-2018 program[28] integrated into the WINGX interface.[29] The positions of the H atoms are geometrically generated via the HFIX instruction included in SHELXL-2014[30] and allowed to ride on their parent atoms with N−H = 0.86 Å and C−H = 0.93; 0.96 or 0.97 Å. It should be noted that the structure contains two disordered atoms in the organic moiety. Indeed, the SHELXL-2014 program[30] indicates that N4 and C24 atoms should be split in two positions. After splitting these two atoms, many refinement cycles by SHELXL-2014 program[30] indicate that there is no atom to be split or in NPD. The final refinement of the structure led to very good reliability factors R_1 = 0.036 and wR_2 = 0.086. Furthermore, all drawings of the crystal structure were made using the Diamond 3.2 program.[31] Table 1 includes the major crystallographic data. Table 2 presents the fractional atomic coordinates and the equivalent isotropic temperature factors. Selected bond distances, angles, and hydrogen bonds are depicted in Tables 3 and 4, respectively.

Table 1. Crystallographic Data and Structure Refinements of $(C_{12}H_{17}N_2)_2[CdBr_4]$

formula	$(C_{12}H_{17}N_2)_2[CdBr_4]$
color/shape	white/prism
formula weight (g mol^{-1})	810.59
crystal system	monoclinic
space group	$P2_1/n$
density	1.806
crystal size (mm)	0.57 × 0.40 × 0.30
temperature (K)	296(2)
diffractometer	Bruker APEXII CCD
a (Å)	13.0098(4)
b (Å)	15.1193(5)
c (Å)	15.5737(4)
β (deg)	103.294(2)
V (Å^3)	2981.24(16)
Z	4
radiation type	Mo $K\alpha$ (0.71073 Å)
absorption correction	multiscan
θ range for data collection (deg)	$1.903 \leq \theta \leq 27.522$
measured reflections	93166
independent reflections	6855
observed data [$I > 2\sigma(I)$]	4797
index ranges	$h = -16 \rightarrow 16$
	$k = -19 \rightarrow 19$
	$l = -20 \rightarrow 20$
F (000)	1576
number of parameters	320
R_1	0.0368
wR_2	0.0863
goof	1.098

https://doi.org/10.1021/acsomega.4c01997
ACS Omega 2024, 9, 28339−28353

Table 2. Fractional Atomic Coordinates and Equivalent Isotropic Temperature Factors (Å^2)

	x	y	z	U_{eq}	occupation
Cd01	0.74758(2)	0.28120(2)	0.50474(2)	0.04484(9)	1
Br02	0.62376(4)	0.20582(3)	0.36996(3)	0.05250(12)	1
Br03	0.83634(4)	0.40463(3)	0.42871(3)	0.05848(14)	1
Br04	0.64787(4)	0.35914(3)	0.60804(3)	0.05887(14)	1
Br05	0.87028(5)	0.17195(4)	0.60029(4)	0.07549(17)	1
N42	0.372(2)	0.4339(7)	0.8696(16)	0.088(7)	0.46
N41	0.3238(7)	0.4397(6)	0.8199(8)	0.044(2)	0.54
C242	0.351(2)	0.3753(14)	0.7159(16)	0.118(8)	0.60
C241	0.382(3)	0.3393(16)	0.7151(17)	0.072(7)	0.40
N1	0.8788(3)	0.5229(2)	0.6248(2)	0.0428(8)	1
N3	0.3977(3)	0.5950(2)	0.7524(2)	0.0463(8)	1
N2	0.8737(3)	0.6508(3)	0.7736(2)	0.0616(11)	1
C18	0.3570(3)	0.5958(3)	0.8296(3)	0.0426(9)	1
C6	0.8046(3)	0.5924(2)	0.6241(3)	0.0390(9)	1
C5	0.8044(3)	0.6510(3)	0.6932(3)	0.0434(9)	1
C7	0.9637(3)	0.4973(3)	0.6801(3)	0.0471(10)	1
C21	0.4598(3)	0.5386(3)	0.7296(3)	0.0482(10)	1
C2	0.6522(3)	0.6632(3)	0.5326(3)	0.0507(11)	1
C19	0.4187(4)	0.3969(3)	0.8014(3)	0.0481(10)	1
C1	0.7276(3)	0.5986(3)	0.5453(3)	0.0471(10)	1
C3	0.6533(4)	0.7241(3)	0.5988(3)	0.0531(11)	1
C4	0.7268(4)	0.7181(3)	0.6768(3)	0.0527(11)	1
C17	0.3335(4)	0.5197(3)	0.8709(3)	0.0579(12)	1
C20	0.5019(3)	0.4645(3)	0.7900(3)	0.0490(10)	1
C9	0.9299(4)	0.5743(3)	0.8176(3)	0.0542(11)	1
C8	1.0076(4)	0.5412(3)	0.7651(3)	0.0614(13)	1
C12	1.0201(4)	0.4178(3)	0.6577(3)	0.0631(13)	1
C22	0.4922(5)	0.5506(3)	0.6452(4)	0.0729(16)	1
C13	0.3396(4)	0.6781(3)	0.8618(4)	0.0671(14)	1
C16	0.2932(4)	0.5307(4)	0.9461(3)	0.0675(14)	1
C15	0.2777(4)	0.6120(4)	0.9770(3)	0.0721(15)	1
C14	0.3008(5)	0.6869(4)	0.9355(4)	0.0857(18)	1
C11	0.8542(5)	0.5007(4)	0.8275(4)	0.0819(17)	1
C10	0.9914(5)	0.6057(4)	0.9076(3)	0.0846(18)	1
C23	0.4691(6)	0.3240(5)	0.8597(6)	0.123(3)	1

2.3. Spectroscopic Measurements. A conventional UV−visible spectrophotometer (HITACHI, U-3300) was used to measure UV−visible light between 200 and 800 nm.

Additionally, we investigated the electrical conduction properties by using a Solartron SI 1260 impedance analyzer. The measurement was influenced by factors such as a temperature range of 363−418 K, a voltage of 0.5 V, and a frequency range of 40 Hz to 5 MHz.

3. RESULTS AND DISCUSSION

3.1. Structural Analysis. The new-centrosymmetric hybrid material with the formula $(C_{12}H_{17}N_2)_2[CdBr_4]$ crystallizes at 296(2) K in the monoclinic system (space group $P2_1/n$) with the following parameters: a = 13.009(4) Å; b = 15.119(5) Å; c = 15.573(4) Å; β = 103.294(2) °; V = 2981.241(6) Å^3 and Z = 4. Its 0D structure is composed of isolated $[CdBr_4]^{2-}$ and protonated amine $(C_{12}H_{17}N_2)^+$. The structure's cohesion is established by N−H···Br hydrogen bonds and C−H···π interactions (Figure 2). It should be noted that the substitution of the halide ions (chlorine by bromine) in $(C_{12}H_{17}N_2)_2[CdX_4]$ (X = Br, Cl) leads to significant structural changes. Indeed, the chlorine-based compound $(C_{12}H_{17}N_2)_2[CdCl_4]$ crystallizes in the triclinic system (space group $P\bar{1}$).[23]

Figure 3 shows the asymmetric unit of $(C_{12}H_{17}N_2)_2[CdBr_4]$. It contains only one cadmium(II) cation, surrounded by four bromide ions, $[CdBr_4]^{2-}$, and two organic cations.

The first one is fully ordered, while the second presents two disordered atoms. Indeed, the N4 nitrogen atom is split into N41 and N42 atoms with refined occupancy levels of 0.54 and 0.46, respectively, while the C24 carbon atom is split into C241 and C242 atoms with refined occupancy levels of 0.4 and 0.6 (Table 2). The cadmium(II) cation, like all other atoms in the unit cell, occupies a generic location (Wyckoff site 4e) and is coupled to four Br^- ions. $[CdBr_4]^{2-}$ has three potential geometries: tetrahedron, square plane, and seesaw geometry. To establish the geometry of the cadmium polyhedron, we estimated the τ_4 parameter (τ_4 = 0 for square plane geometry and τ_4 = 1 for tetrahedron shape) using the following formula:[32]

$$\tau_4 = 360 - \frac{\alpha + \beta}{360 - 2\theta} \quad (1)$$

With α and β being the two big angles in the polyhedron and θ being the angle in a regular tetrahedron, θ = 109.5°.

In our situation, using α = 116.58° and β = 113.47°, the τ_4 parameter is calculated as 0.921. This research reveals that the cadmium atom's polyhedron has a tetrahedral geometry.

https://doi.org/10.1021/acsomega.4c01997
ACS Omega 2024, 9, 28339−28353

Table 3. Selected Bond Distances (Å) and Angles (deg)

distances (Å)		angles (deg)	
Cd01−Br05	2.5295(6)	Br05−Cd01−Br04	105.79(2)
Cd01−Br04	2.5727(5)	Br05−Cd01−Br02	112.28(2)
Cd01−Br02	2.5971(5)	Br04−Cd01−Br02	113.47(2)
Cd01−Br03	2.6167(6)	Br05−Cd01−Br03	116.58(2)
N42−C17	1.390(13)	Br04−Cd01−Br03	107.142(19)
N42−C19	1.455(12)	Br02−Cd01−Br03	101.739(18)
N41−C17	1.436(10)	C17−N42−C19	125.4(11)
N41−C19	1.480(9)	C17−N41−C19	120.3(6)
C19−C242	1.45(2)	C7−N1−C6	134.4(4)
C19−C241	1.58(2)	C21−N3−C18	128.5(4)
N1−C7	1.293(5)	C5−N2−C9	126.0(4)
N1−C6	1.425(5)	C13−C18−C17	120.6(4)
N3−C21	1.280(5)	C13−C18−N3	116.0(4)
N3−C18	1.420(5)	C17−C18−N3	123.4(4)
N2−C5	1.365(5)	C5−C6−C1	120.5(4)
N2−C9	1.453(6)	C5−C6−N1	125.7(4)
C18−C13	1.379(6)	C1−C6−N1	113.8(4)
C18−C17	1.386(6)	N2−C5−C6	126.1(4)
C6−C5	1.394(6)	N2−C5−C4	117.5(4)
C6−C1	1.397(6)	C6−C5−C4	116.4(4)
C5−C4	1.413(6)	N1−C7−C8	123.9(4)
C7−C8	1.475(6)	N1−C7−C12	118.5(4)
C7−C12	1.491(6)	C8−C7−C12	117.6(4)
C21−C22	1.481(6)	N3−C21−C22	119.5(4)
C21−C20	1.484(6)	N3−C21−C20	119.4(4)
C2−C1	1.366(6)	C22−C21−C20	121.1(4)
C2−C3	1.381(6)	C1−C2−C3	119.0(4)
C19−C23	1.482(7)	C242−C19−N42	119.2(18)
C19−C20	1.529(6)	C242−C19−C23	118.9(10)
C3−C4	1.365(6)	N42−C19−C23	92.3(9)
C17−C16	1.399(7)	N41−C19−C23	118.5(6)
C9−C11	1.517(7)	C242−C19−C20	109.8(9)
C9−C10	1.522(7)	N42−C19−C20	104.9(8)
C9−C8	1.523(7)	N41−C19−C20	112.0(4)
C13−C14	1.364(7)	C23−C19−C20	110.1(4)
C16−C15	1.351(7)	N41−C19−C241	107.5(12)
C15−C14	1.370(8)	C23−C19−C241	96.7(11)
		C20−C19−C241	110.8(11)
		C2−C1−C6	121.4(4)
		C4−C3−C2	120.3(4)
		C3−C4−C5	122.3(4)
		C18−C17−N42	130.6(6)
		C18−C17−C16	117.0(4)
		N42−C17−C16	109.1(7)
		C18−C17−N41	116.3(6)
		C16−C17−N41	124.2(6)
		C21−C20−C19	114.2(4)
		N2−C9−C11	111.4(4)
		N2−C9−C10	106.6(4)
		C11−C9−C10	110.5(4)
		N2−C9−C8	109.4(4)
		C11−C9−C8	109.9(4)
		C10−C9−C8	108.9(4)
		C7−C8−C9	117.5(4)
		C14−C13−C18	121.1(5)
		C15−C16−C17	121.5(5)
		C16−C15−C14	121.1(5)
		C13−C14−C15	118.7(5)

Table 4. Hydrogen Bonding Geometry (Å, °)

D—H···A	D—H	H···A	D···A	D—H···A
N42-HN42···Br05[a]	0.86	3.11	3.936(18)	162.9
N41-HN41···Br02[a]	0.86	2.96	3.627(8)	135.6
N1-HN1···Br03	0.86	2.62	3.472(3)	172.8
N3-HN3···Br02[b]	0.86	2.71	3.541(3)	161.9
N2-HN2···Br04[c]	0.86	2.87	3.693(4)	161.2

[a]Symmetry codes: $x - 1/2, -y + 1/2, z + 1/2$. [b]$-x + 1, -y + 1, -z + 1$. [c]$-x + 3/2, y + 1/2, -z + 3/2$.

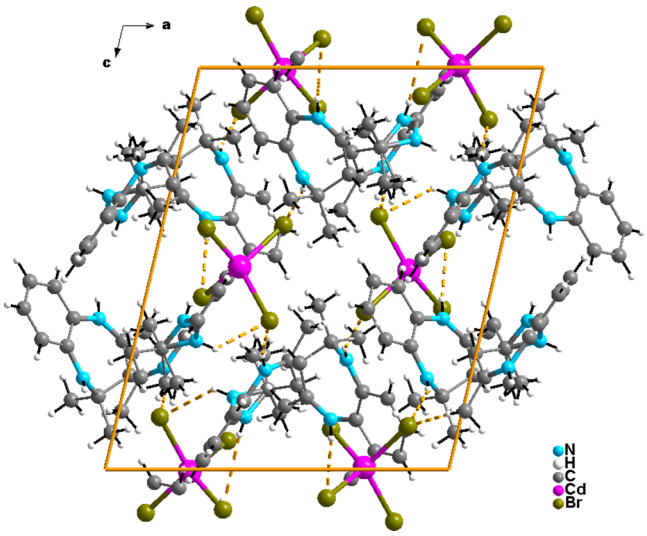

Figure 2. Projection of the structure of $(C_{12}H_{17}N_2)_2[CdBr_4]$ along the crystallographic *b*-axis.

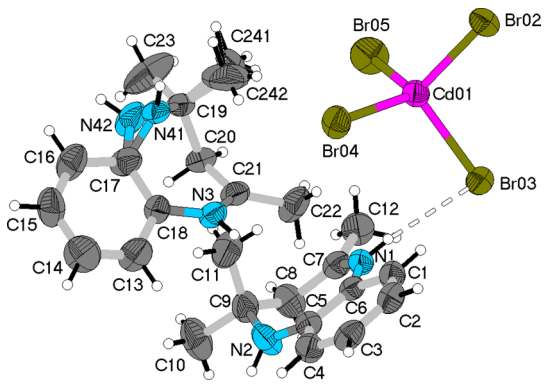

Figure 3. Asymmetric unit of $(C_{12}H_{17}N_2)_2[CdBr_4]$. Displacement ellipsoids are drawn at the 50% probability level. Hydrogen bonds are represented by dashed lines.

Tetrabromocadmate (II) anions $[CdBr_4]^{2-}$ produce anionic pseudolayers parallel to the (0 0 1) plane at z = 0 and z = 1/2 when stacked along the a and b crystallographic axes (Figures 2 and 4). These metallic tetrahedra have a minimum intermetallic Cd−Cd distance of 8.9746(4) Å. The Cd−Br distances in the $[CdBr_4]^{2-}$ tetrahedra range from 2.5295(6) to 2.6167(6) Å, whereas the Br−Cd−Br angles range from 101.73(18) to 116.58(2)° (Table 3).

The tetrabromocadmate (II) anions $[CdBr_4]^{2-}$ are stacked one over the other along the *a* and *b* crystallographic axes in a manner that they form anionic pseudolayers parallel to the (0 0 1) plane (Figures 2 and 4) at $z = 0$ and $z = 1/2$. These metallic tetrahedra are separated from each other with a minimum

https://doi.org/10.1021/acsomega.4c01997
ACS Omega 2024, 9, 28339−28353

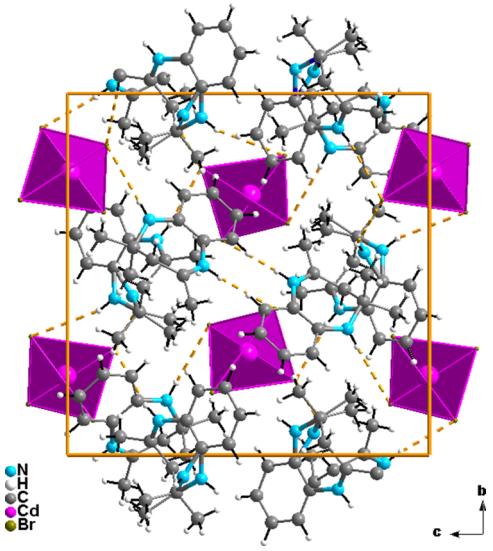

Figure 4. Projection of the structure of $(C_{12}H_{17}N_2)_2[CdBr_4]$ along the crystallographic *a*-axis.

intermediate Cd−Cd distance equal to 8.9746(4) Å. Within the $[CdBr_4]^{2-}$ tetrahedra, the Cd−Br distances range from 2.5295(6) to 2.6167(6) Å while the Br−Cd−Br angles vary between 101.73(18) and 116.58(2)° (Table 3). These values are consistent with those observed in other compounds containing $CdBr_4$ tetrahedra, such as $(CH_3NH_3)_2CdBr_4$ and $(C_5H_6N_2Cl)_2[CdBr_4].H_2O$.[33−35] Taking into account these distances and angles and using the distortion equations indices (DI) of Baur:[36]

$$\mathrm{DI(Cd-Br)} = \sum_{i=1}^{n_1} \frac{|d_i - d_m|}{4d_m};\ \mathrm{DI(Br-Cd-Br)} = \sum_{i=1}^{n_2} \frac{|a_i - a_m|}{6a_m} \quad (2)$$

where, d = Cd−Br distance, a = Br−Cd−Br angle and m = average value.

The estimated distortion indices DI (Cd−Br) = 0.0107(1) and DI (Br−Cd−Br) = 0.036(1) indicate that the $CdBr_4$ tetrahedron is slightly distorted from the conventional tetrahedron. This is attributed to the presence of intermolecular hydrogen-bonding interactions of the type N−H···Br, which ensure the material's cohesion. The negative charges of the cadmium tetrahedra $[CdBr_4]^{2-}$ are compensated by the protonated amines $(C_{12}H_{17}N_2)^+$ which filled the space between the inorganic metallic anions (Figures2 and 4). The principal lengths and angles of the protonated amines are shown in Table 3. C−N and C−C lengths are comparable to those observed in other similar derivates. The structure is stabilized via N−H···Br hydrogen bonding between the protonated amines and the inorganic tetrahedra, as well as C−H···π interactions between the protonated amine aromatic rings. The organic cations create a T-shaped conformation due to perpendicular aromatic−aromatic interactions between benzene rings.[37] The dihedral angle between the planes of two T-shaped aromatic rings is 67.87(14)° and the centroid-to-centroid distance is 5.5134 Å, which is close enough to allow C−H···π interactions at a distance of 3.098 Å (Figure 5). In Figure 6, organic cations form N−H···Br hydrogen bonds with two $CdBr_4$ tetrahedra using their ammonium group

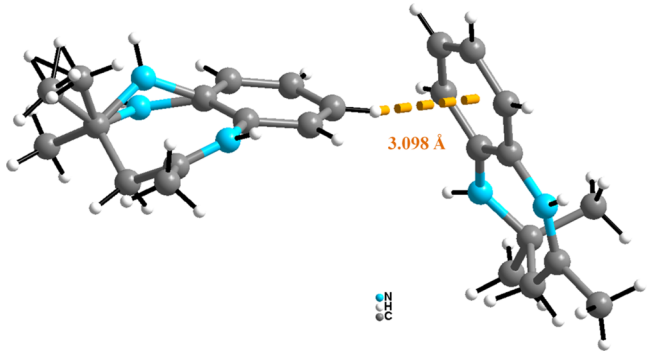

Figure 5. C−H···π interactions in the structure of $(C_{12}H_{17}N_2)_2[CdBr_4]$.

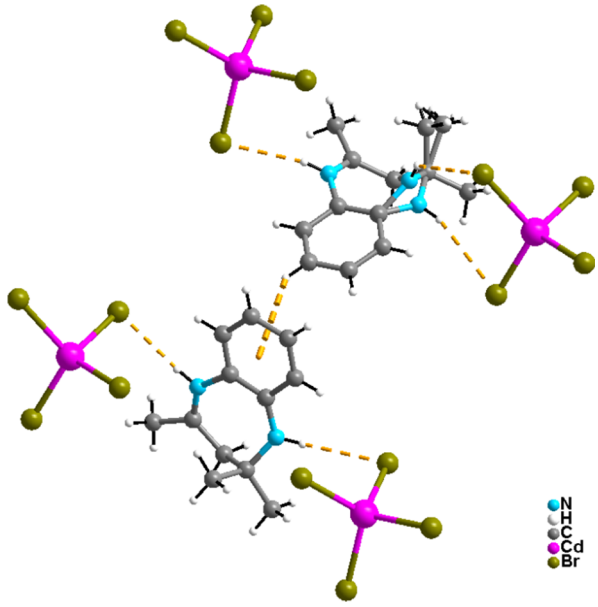

Figure 6. Hydrogen bonds were established by the protonated amine in $(C_{12}H_{17}N_2)_2[CdBr_4]$.

hydrogen atoms. Table 4 shows that intermolecular hydrogen bonds have N···Br lengths ranging from 3.472(3) to 3.936(18) Å and N−H···Br angles between 135.6 and 172.8°.

3.2. Optical Properties. The absorption spectrum of the title compound $(C_{12}H_{17}N_2)_2[CdBr_4]$ (blue line) is depicted in Figure 7a. Lasers, solar cells, photovoltaics, photoluminescence, and diodes all rely heavily on the optical band gap.[38−40] One of the most noticeable aspects of hybrid materials is the optical band gap, which can be direct or indirect.[41]

Generally, the optical absorption coefficient (α) of the compound and the evaluation of the absorption spectra are used to experimentally identify the nature of the bandgap transition in semiconductor materials. The Beer−Lambert law[42] correlates with cell thickness (e), making absorption measurements (A) a suitable tool for calculating α.

$$\alpha = \frac{2.303 \times A}{e} \quad (3)$$

The equation that follows serves as an illustration of the Tauc relationship, which connects α to photon energy (hv) and the optical band gap (E_g).[43,44]

https://doi.org/10.1021/acsomega.4c01997
ACS Omega 2024, 9, 28339−28353

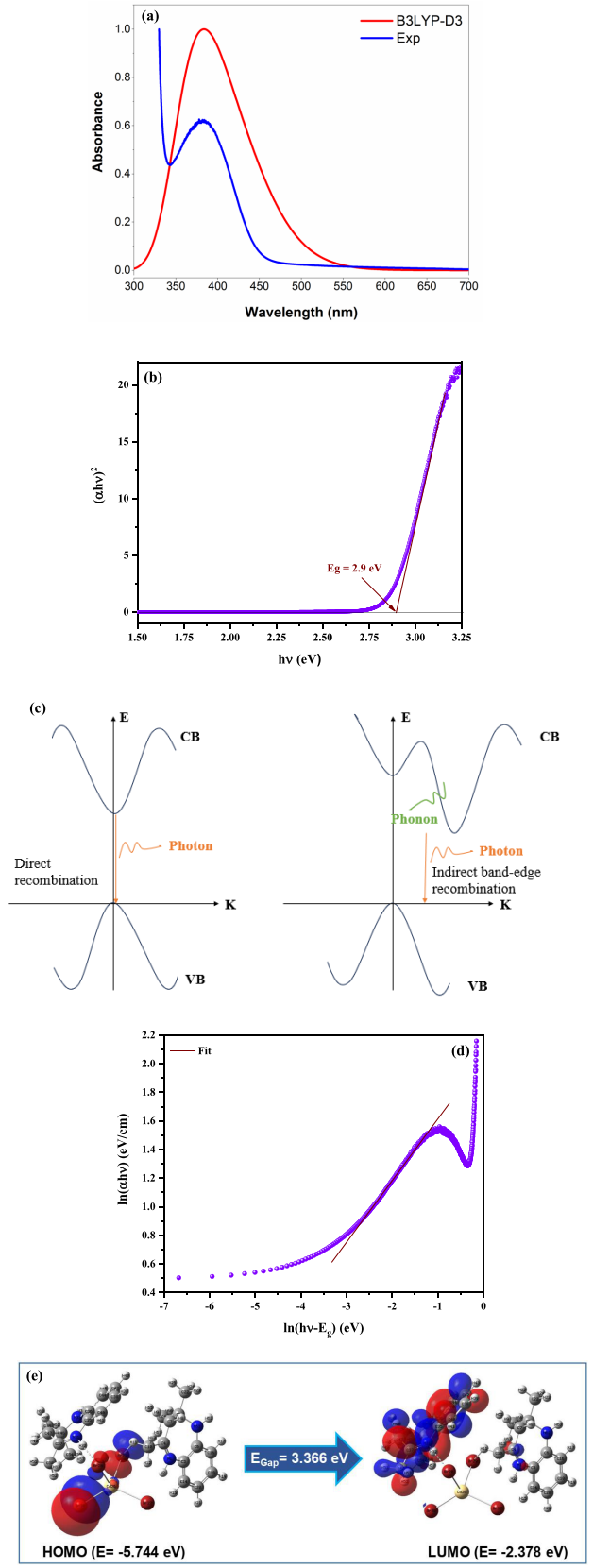

Figure 7. (a) Experimental and predicted UV−vis spectra of $(C_{12}H_{17}N_2)_2[CdBr_4]$. (b) Tauc plot for $(C_{12}H_{17}N_2)_2[CdBr_4]$. (c) Direct and indirect band gaps. (d) Plot of $\ln(\alpha h\nu)$ vs $\ln(h\nu - E_g)$. (e) HOMO and LUMO frontier orbital iso surfaces of $(C_{12}H_{17}N_2)_2[CdBr_4]$.

$$\alpha = \frac{\beta}{h\nu}(h\nu - E_g)^n \tag{4}$$

where n is the power factor that denotes the transition mode and the constant β denotes the degree of disorder. Typically, the bandgap transition takes one of two values: 1/2 or 2, depending on whether it is allowed or forbidden and whether it is direct or indirect. While photon absorption and emission occur through permitted transitions in direct bandgap semiconductors (n = 1/2), absorption and recombination in indirect bandgap semiconductors result in the production of both photons and phonons (Figure 7b). The following Tauc formula is used to determine the bandgap E_g:

$$(\alpha h\nu)^{1/n} = \beta(h\nu - E_g) \tag{5}$$

The most acceptable and satisfying plot is produced for n = 1/2 after plotting $(\alpha h\nu)^2$ and $(\alpha h\nu)^{1/2}$ as functions of photon energy $(h\nu)$. In compliance with the Tauc equation, the direct transition has been selected.

$$(\alpha h\nu)^2 = \beta(h\nu - E_g) \tag{6}$$

As shown in Figure 7c, projecting the linear part to $(\alpha h\nu)^2$ = 0 can be used to determine the bandgap E_g value. E_g is found to be comparable to 2.9 eV. This value is lower than those found in $(C_{12}H_{17}N_2)_2[ZnBr_4]$ (3.76 eV).[45] The exchange of zinc by cadmium changes the interatomic distances in the crystal lattice. This causes a shift in the locations of the valence and conduction bands, leading to a drop-in gap energy from 3.76 to 2.9 eV. Therefore, $(C_{12}H_{17}N_2)_2[CdBr_4]$ is a suitable contender for optoelectronics.[46] The subsequent equation is employed to verify the transition mode of the optical band:[47]

$$\ln(\alpha h\nu) = \ln(\beta) + n\ln(h\nu - E_g) \tag{7}$$

As a result, Figure 7d depicts the graph of $\ln(\alpha h\nu)$ plotted against $\ln(h\nu - E_g)$. The slope of this curve determines the power factor (n), which serves to identify the optical transition mode. Figure 7d and eq 7 show the following linear relationship:

$$\ln(\alpha h\nu) = 2.06 + 0.5\ln(h\nu - 2.9);\ (n = \frac{1}{2}) \tag{8}$$

It is therefore confirmed that our material's direct optical band transition mode exists. n is nearly equivalent to 1/2, consistent with the anticipated mode.

Electronic characteristics, including the HOMO−LUMO orbital isosurfaces, excitation energies, absorption wavelengths, and oscillator strengths, were calculated at the TD-DFT/B3LYP-D3/LanL2DZ theoretical level using the Gaussian G09 software.[48−52] GaussView visualization software is used for both the creation of input files and the examination of the results. Figure 7a shows the computed UV−vis spectra (red line). In Table 5, the oscillator strengths (f), absorption wavelengths (λ), excitation energies (E), and primary contributions of the transitions produced by the GaussSum program are grouped.

Observably, the predicted absorption occurs within the range of approximately 300−550 nm, and the intense absorption is found to be close to 384 nm, which is in good agreement with observed absorption. In Table 5, it is noted that the greatest oscillator strength measures f = 0.0414 au, observed at 373 nm. This measurement signifies the relative intensity of light absorption or emission at that specific

https://doi.org/10.1021/acsomega.4c01997
ACS Omega 2024, 9, 28339−28353

Table 5. Calculated Absorption Wavelength λ, Excitation Energies E and Oscillator Strengths f Using the TD-DFT Method at the B3LYP-D3/LanL2DZ Level of Theory in the Gas Phase[a]

no.	E (eV)	λ (nm)	f (a.u)	major contribution
1	270	445	0.0008	H → L (98%)
2	278	432	0.0348	H-2→L (14%), H-1→L (83%)
3	283	425	0.0045	H-2→L (80%), H-1→L (14%)
4	288	417	0.0028	H-2→L+1 (38%), H-1→L+1 (28%), $\vec{H}$L +1 (19%)
5	290	413	0.0044	H-3→L (21%), H-3→L+1 (26%), H-2→L +1 (23%)
6	293	410	0.0032	H-3→L (69%), H-3→L+1 (11%), $\vec{H}$L+1 (11%)
7	304	394	0.0001	H-3→L+1 (44%), $\vec{H}$L+1 (44%)
8	309	388	0.0011	H-2→L+1 (26%), H-1→L+1 (63%)
9	312	385	0.0033	H-6→L (77%)
10	312	384	0.0260	H-5→L (61%), H-4→L (32%)
11	321	374	0.0353	H-6→L+1 (11%), H-4→L+1 (63%)
12	322	373	0.0414	H-7→L+1 (54%), H-6→L+1 (15%), H-4→L+1 (14%)
13	327	367	0.0043	H-6→L+1 (53%), H-5→L+1 (12%)
14	328	366	0.0018	H-7→L (47%), H-6→LUMO (11%), H-4→L (13%)
15	330	364	0.0015	H-8→LUMO (29%), H-5→L (10%), H-4→L (28%)

[a]H: HOMO; L: LUMO.

wavelength, typically linked to an electronic or molecular transition within a chemical system. Therefore, the title compound could be relevant for studying the optical properties of materials or specific chemical reactions.

Figure 7e depicts the frontier orbitals of HOMO and LUMO. The HOMO orbitals, situated at −5.744 eV, are predominantly localized within inorganic group $CdBr_4$. Despite this, the LUMO orbitals, located at −2.378 eV, primarily encompass the organic group. As multiple earlier investigations have shown, the energy gap between the highest occupied molecular orbital (HOMO) and the lowest unoccupied molecular orbital (LUMO), commonly referred to as the HOMO−LUMO gap, is indeed a crucial parameter in determining a compound's kinetic stability and chemical reactivity.

A smaller HOMO−LUMO gap indicates that electrons can be more easily promoted from the HOMO to the LUMO, resulting in higher reactivity and potentially faster reaction rates. Conversely, a larger HOMO−LUMO gap suggests greater kinetic stability as electron transitions require more energy and are less likely to occur spontaneously.

The HOMO → LUMO transition occurs at 445 nm with a low oscillator strength. As a result, a compound with a narrow gap energy exhibits heightened polarizability, augmented chemical reactivity, and decreased kinetic stability, thus being categorized as a "soft" molecule.[53−55] The energy gap between the HOMO and LUMO orbitals of the compound under investigation is 3.366 eV. This lower value enhances the reactivity of the molecule.

The global chemical reactivity descriptors, such as hardness (η), chemical potential (μ), softness (S), electronegativity (χ), and electrophilicity index (ω), have been computed using the following equations: $\eta = (IP - EA)/2$, $\mu = -(IP + EA)/2$, $S = 1/2\eta$, $\chi = (IP + EA)/2$ and $\omega = \mu^2/2\eta$, where IP (IP = $-E_{HOMO}$) and EA (EA = $-E_{LUMO}$) are the ionization potential and electron affinity, respectively. Electron affinity is the amount of energy necessary for a neutral molecule to accept one electron from a donor. Table 6 shows that the title compound's ionization potential and electron affinity are 5.744 and 2.378 eV, respectively. The computed values for global hardness, global softness, chemical potential, and global electrophilicity index are 1.683, 1.188, −4.096, and 8.245 eV (Table 6), respectively. The molecule's low chemical potential and high global electrophilicity index indicate its significant electrophilic nature. The high electrophilicity index indicates a great tendency or capacity of a molecule or species to act as an electrophile. This suggests that the entity in question exhibits a strong affinity or readiness to accept or react with electron-rich species or nucleophiles in a chemical reaction. A higher electrophilicity index often signifies a greater reactivity toward nucleophilic attack or electron donation.

Table 6. TD/B3LYP-D3/LanL2DZ Calculations of HOMO-LUMO Energy Gap, Chemical Potential, Electronegativity, Global Hardness, Global Softness, Electrophilicity Index, and Dipole Moment Performed in the Gas Phase

function	value
E_{HOMO} (eV)	−5.744
E_{LUMO} (eV)	−2.378
$\Delta E_{HOMO-LUMO\ gap}$ (eV)	3.366
E_{HOMO-1} (eV)	−5.823
E_{LUMO+1} (eV)	−2.253
$\Delta E_{HOMO-1-LUMO+1\ gap}$ (eV)	3.570
chemical potential μ (eV)	−4.096
electronegativity χ (eV)	4.096
global hardness η (eV)	1.683
global softness ζ $(eV)^{-1}$	1.188
global electrophilicity index (ψ)	8.245
dipole moment (Debye)	17.59

In addition, the dipole moment is found to be 17.59 D, which indicates a relatively strong polarity or asymmetric charge distribution within the title compound. This value suggests that the molecule possesses a notable separation of positive and negative charges, resulting in a substantial overall dipole moment. Besides, as the dipole moment increases, so does the degree of asymmetry in the distribution of charges within the molecule, indicating stronger polarity. This property often influences the molecule's behavior in various chemical and physical interactions, such as its interactions with electric fields, solvents, or other polar molecules.

Our analysis found that the sample's bandgap energy values are higher than the projected threshold ($\lambda > 1.23$ eV) for water separation. In the context of sunlight's photocatalysis, this discovery is extremely significant. Because of its unique characteristics relating to the high band gap, this sample functions as a photocatalyst, able to absorb photons from sunshine. Photons that are absorbed produce electron−hole pairs when their energy surpasses the band gap. The reactive species in charge of photocatalysis processes are these electron−hole pairs. These reactive species possess the capability to split water into hydrogen and oxygen, thereby aiding in the generation of clean, sustainable energy.[56]

3.3. omplex Impedance Spectroscopy Study. The modeling process for complex impedance is highly useful in distinguishing between the impacts of electrodes, grains, and grain boundaries. Furthermore, it provides important insights

https://doi.org/10.1021/acsomega.4c01997
ACS Omega 2024, 9, 28339−28353

into the relaxation and polarization processes of space charges by assigning distinct measurements of resistance and capacitance to the actions of grains and grain boundaries in the material under investigation.[57,58]

Figure 8 shows the Nyquist plots of hybrid $(C_{12}H_{17}N_2)_2[CdBr_4]$ throughout a temperature range of 363

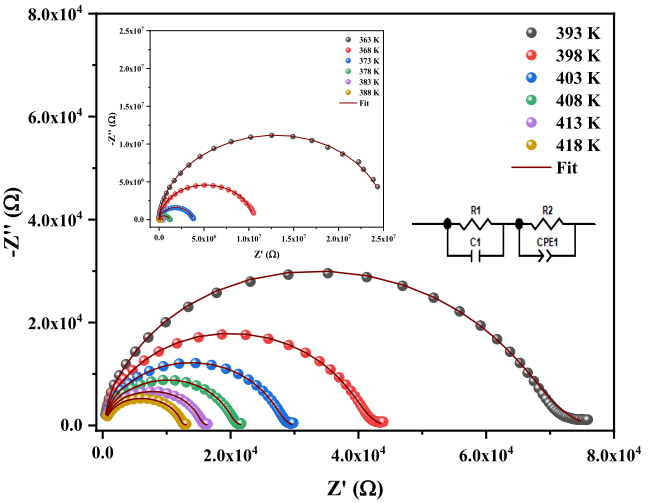

Figure 8. Nyquist plot $(C_{12}H_{17}N_2)_2[CdBr_4]$ at different temperatures, inset Maxwell–Wagner equivalent circuit.

to 418 K. The spectra display a single, depressed semicircular arc at all temperatures. The decreasing trends in the radii of these semicircular arcs with temperature suggest the occurrence of thermally induced relaxation processes.[59]

The Zview program was employed to match the observed impedance measurement with a standard equivalent circuit consisting of two parallel elements, R–C (grain effect) and R–Q (grain boundary effect), arranged in series, as depicted in the inset of Figure 8. The Constant Phase Element (CPE) is utilized in the equivalent circuit to compensate for nonideal capacitance behavior that might occur due to the presence of numerous relaxation phenomena in the $(C_{12}H_{17}N_2)_2[CdBr_4]$ system with nearly equal or comparable relaxation periods.[60,61] The formula for CPE's capacitance is[62]

$$Z_{CPE} = \frac{1}{Q(j\omega)^{\alpha}} \tag{9}$$

Equation 9 uses the parameter α $(0 \leq \alpha \geq 1)$ to approximate the departure from Debye-type behavior in the relaxation mechanism. It equals zero for purely resistive behavior and unity for capacitive behavior.

The impedance data for $(C_{12}H_{17}N_2)_2[CdBr_4]$ was calibrated using the equivalent circuitry, as illustrated by the solid line in Figure 8. The theoretical line, calculated from the predicted values, fits the experimental data rather well. Figure 9a,b presents the retrieved parameters for the circuit components.

Figure 9a shows the variation as a function of temperature of the resistance associated with both the grain (R_1) and grain border (R_2). Notably, the resistance near the grain border exceeds that of the grain itself. Typically, the increased disorder and instability in the atomic arrangement at grain boundaries lead to the growth of the grains at high temperatures.[63] As a result, the resistance of both the grain and the grain boundary decreases with increasing temperature.

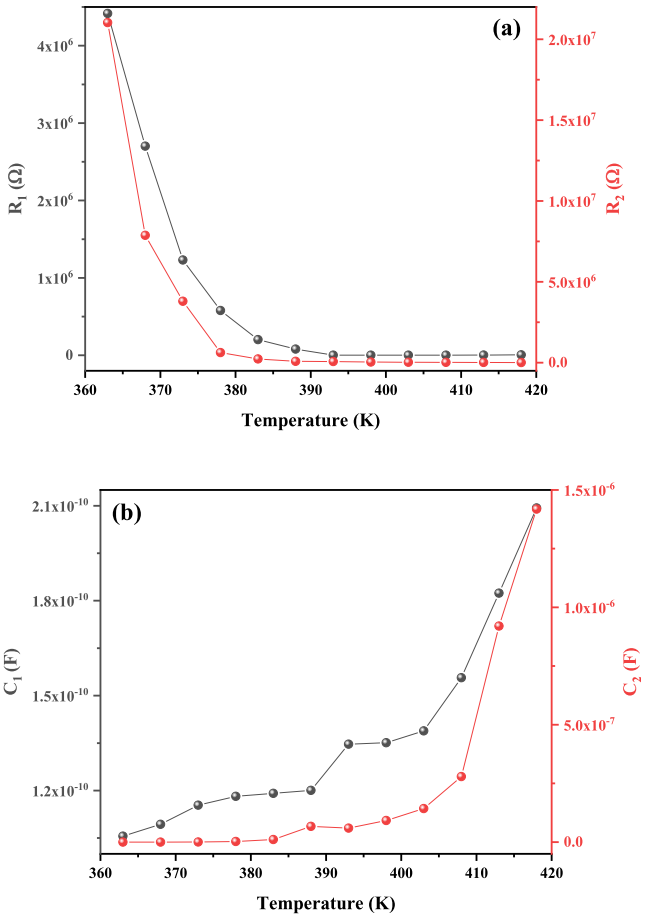

Figure 9. (a) Variation of R_1 (resistance of grain) and R_2 (resistance of grain boundary) with temperatures. (b) Variation of C_1 (capacitance of grain) and C_2 (capacitance of grain boundary) with temperatures.

Furthermore, an increase in temperature leads to a slight increase in the capacitance of both the grain and its boundary (Figure 9b). The intrinsic dielectric constant (ε_{gb}) and the width and surface of the barrier layer (d and A, respectively) determine the grain boundary capacitance $(C_{gb} = \varepsilon_{gb}A/d)$. As the temperature increases, there is an increase in free ions at the interfaces, resulting in a decrease in the width of the barrier layer. The width of the layer at grain boundaries is determined by the ratio of the trapped to free ion density. The density of trapped ions decreases as temperature increases, which suggests depopulation, but the density of free ions increases, resulting in a decrease in the barrier layer.[64]

The complex impedance formalism was quantitatively stated as

$$Z(\omega) = Z'(\omega) + iZ''(\omega) \tag{10}$$

where Z' and Z'' denote their standard expressions as described above

$$Z' = \frac{R_1}{(1 + (R_1C_1\omega)^2)} + \frac{R_2^{-1} + Q_2\omega^{\alpha_2}\cos(\frac{\alpha_2\pi}{2})}{(R_2^{-1} + Q_2\omega^{\alpha_2}\cos(\frac{\alpha_2\pi}{2}))^2 + (Q_2\omega_2^{\alpha}\sin(\frac{\alpha_2\pi}{2}))^2} \tag{11}$$

https://doi.org/10.1021/acsomega.4c01997
ACS Omega 2024, 9, 28339−28353

$$-Z'' = \frac{R_1C_1\omega}{(1 + (R_1C_1\omega)^2)} + \frac{C_2\omega + Q_2\omega^{\alpha_2} + Q_2\omega^{\alpha_2}\sin(\frac{\alpha_2\pi}{2})}{(R_2^{-1} + Q_2\omega^{\alpha_2}\cos(\frac{\alpha_2\pi}{2}))^2 + (Q_2\omega_2^{\alpha}\sin(\frac{\alpha_2\pi}{2}))^2} \quad (12)$$

The theoretical equations (eqs 11 and 12) generated by the equivalent circuit were utilized to determine the actual values of (Z') and (Z''). Figure 10a,b exhibits the frequency-dependence relationship between Z' and Z'' across the given temperature range (363−418 K). Both real and imaginary impedances exhibit remarkable congruence in their actual (scatter) and theoretical (line) curves at each temperature. As a result, the proposed circuit is suitable for the selected temperature range.

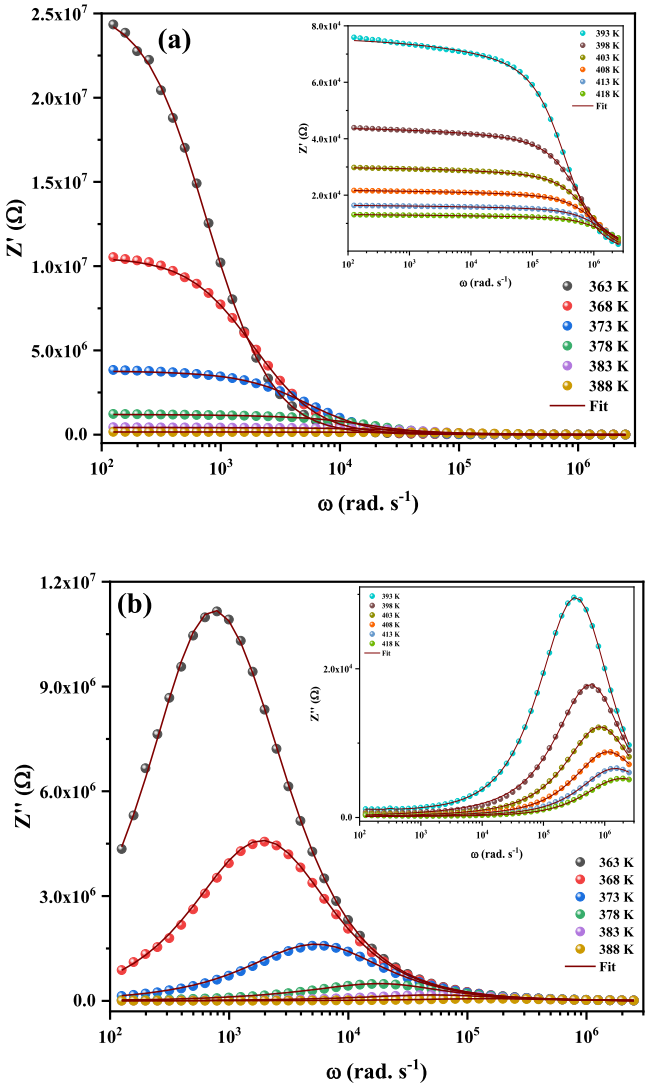

Figure 10. Variation of (a) the real part (Z') and (b) the imaginary part (Z'') of the impedance as a function of angular frequency at several temperatures.

Figure 10a shows that Z' is shown to drop as frequency and temperature increase, demonstrating the compound's negative temperature coefficient of resistance (NTCR)-type behavior.[65,66] This type of behavior suggests that an improvement in ac conductivity may be conceivable due to an increase in charge carrier mobility, as well as a decrease in the trapped charge density in $[C_{12}H_{17}N_2]_2CdBr_4$. In the high-frequency range, Z' becomes independent of temperature, which suggests the presence of space charge in the sample. With higher frequencies, the space charge has less time to relax, leading to a merging of curves at high frequencies. This merging is attributed to a decrease in space charge polarization.[67]

In contrast, the fluctuation of the imaginary portion Z'' (Figure 10b) reveals the essential charge transport mechanism as well as the temperature-dependent relaxation process in $[C_{12}H_{17}N_2]_2CdBr_4$. At low temperatures, the relaxing process appears to be caused by stationary species or electrons, but at high temperatures, flaws or vacancies are responsible. Each spectrum has a distinct peak that has been called the "relaxation frequency." The broad peak deviates significantly from the ideal Debye nature. The localized carriers' motion above the relaxation frequency is influenced by the long-range motion of charge carriers, which is primarily what drives transportation below the loss peak frequency. The relaxation peak's shift toward the high-frequency regime with increasing temperature indicates a thermally dependent relaxation process. Additionally, the peak height decreases as the temperature rises, indicating a reduction in grain and grain boundary resistance.[64]

The Z' and Z'' behavior of our sample in the frequency range is consistent with other hybrid systems in the literature.[45]

3.4. AC Electrical Conductivity. The investigation into electrical conductivity behavior aimed to gain deeper insights into material properties and their significance in electronic devices, and to elucidate the nature of the transport mechanism and interactions of charge carriers.[68] Jonscher attempted to use the following law to explain how ac conductivity behaves:[69]

$$\sigma_{ac}(\omega) = \sigma_{dc} + A\omega^s \quad (13)$$

where σ_{dc} is the frequency-independent part of ac conductivity, A is a temperature-dependent constant, and s denotes the frequency exponent, which is temperature- and material-dependent. The exponent s has a value between 0 and $s < 1$. This behavior is linked to relaxation owing to electron hopping or tunneling between equilibrium locations. However, in the frequency range 1 MHz, experimentally observed values for $s > 1$ have been observed in a variety of disordered materials.

Figure 11a shows plots of the ac conductivity vs frequency across the given temperature range (363−418 K). Frequency dependency in AC conductivity can be contributed by both free and bound carriers. If free carriers are responsible for conduction, the AC conductivity decreases as frequency increases.[69] However, in our case, the measured AC conductivity decreases as the frequency is decreased, suggesting a connection to bound carriers trapped within the material. The increased conductivity with rising frequency can be explained by phenomena such as hopping conduction, the Schottky barrier at the metal-dielectric interface, and Maxwell−Wagner-type conduction.[69]

A closer study of the conductivity plots reveals that the curves exhibit high-frequency dispersion, which follows Jonscher's power law eq (eq 13). According to Jonscher, the frequency dependence of the conductivity is the product of relaxation processes generated by mobile charge carriers. When a mobile charge jumps from one site to another, it remains in

https://doi.org/10.1021/acsomega.4c01997
ACS Omega 2024, 9, 28339−28353

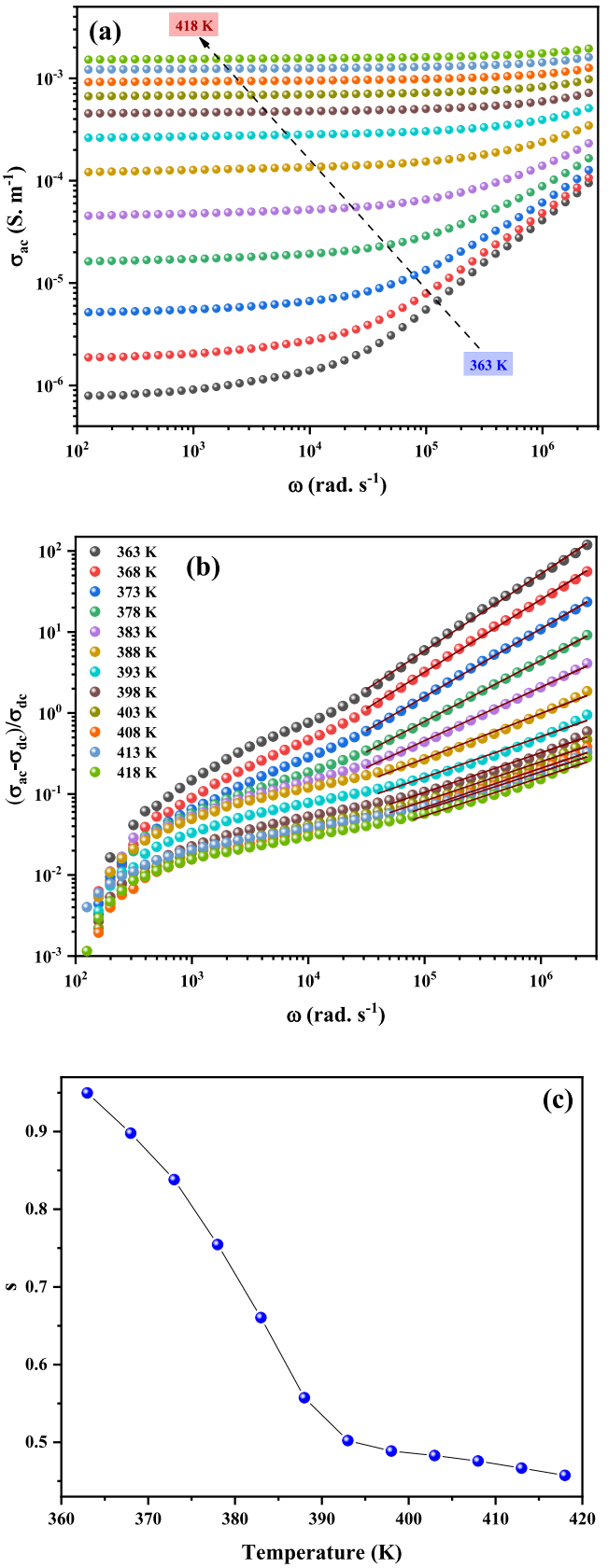

Figure 11. (a) Frequency dependence of ac conductivity at several temperatures. (b) $(\sigma_{ac} - \sigma_{dc})/\sigma_{dc}$ vs frequency plots at different temperatures. (c) Temperature dependence of exponents s.

the state of displacement between two potential energy minima.[70]

It is crucial to investigate the frequency and temperature correlations of the frequency exponents in order to fully comprehend the AC conduction process. Several microscopic models have been created to better understand material conduction processes (QMT, CBH, SPT, and OLPT).[71−74]

When studying ac conductivity data, Nowick et al.[75] utilize a plot of normalized conductivity vs frequency to determine the Jonscher power exponent (s) for reducing DC conductivity effects. The normalized conductivity versus frequency (Figure 11b), illustrates the frequency dependence of ac conductivity with a single linear area with slope s. s is the parameter that defines the interaction between charge carriers involved in the polarization process.

In contrast, the interaction rises with temperature, resulting in a decrease in s from 0.95 to 0.45 (Figure 11c), indicating a correlated barrier hopping (CBH) conduction mechanism. Furthermore, these figures suggest that the system is not in a Debye-type state ($s = 1$).[76] On the other hand, the exponent s is computed at various frequencies using the derivative approach described with[75]

$$s(\omega) = \frac{d(\log(\sigma_{ac}))}{d(\log(\omega))} \tag{14}$$

The representative plots at various frequencies and temperatures of exposent s are shown in Figure 12a,b. At a fixed frequency (Figure 12a), the variance in s decreases with increasing temperature, whereas s increases with increasing temperature (Figure 12b). Therefore, the observed s (ω, T) behavior is characteristic of a CBH-type conduction mechanism. In this context, the dc conductivity data is shown as $\ln(\sigma_{dc})$ vs $1000/T$ at 363−418 K (Figure 13), exhibiting Arrhenius-type behavior as stated by

$$\sigma_{dc} = \sigma_0 \exp\left(-\frac{E_a}{k_B T}\right) \tag{15}$$

where σ_0 is the pre-exponential factor, E_a is the activation energy and k_B is the Boltzmann constant.

Two areas with two activation energies can be distinguished: E_{a1} = 2.53 eV in the range [363−388 K], and E_{a2} = 0.92 eV in the range [388−418 K], which relates to Br^- ionic hopping. It is therefore likely that the observed alteration results from a modification of the conduction mechanism. In the temperature range of 363−388 K, a high activation energy value denotes band-type conduction.[77] The compounds $(C_{12}H_{17}N_2)_2[CdBr_4]$ and $(C_{12}H_{17}N_2)_2[CdCl_4]$ have different activation energies. Therefore, this discrepancy may precisely be described at the level of the inorganic entity $[CdX_4]^{2-}$ (X = Cl, Br) due to the structural differences between these two molecules.

Additionally, dc conductivity at various temperatures varies between 10^{-6} and 10^{-3} S m^{-1}, demonstrating the compound's higher performance, which can be classed as a semiconductor. This finding explains the weak gap energy discovered by studying the optical characteristics.

3.5. Dielectric Properties. Figure 14 displays the frequency-dependent real dielectric constant values (ε') at various temperatures. The materials that were created exhibited higher ε' values at low frequencies, suggesting that they would be suitable low-frequency energy storage candidates.[78,79] Additionally, the values of ε' grow when the

https://doi.org/10.1021/acsomega.4c01997
ACS Omega 2024, 9, 28339−28353

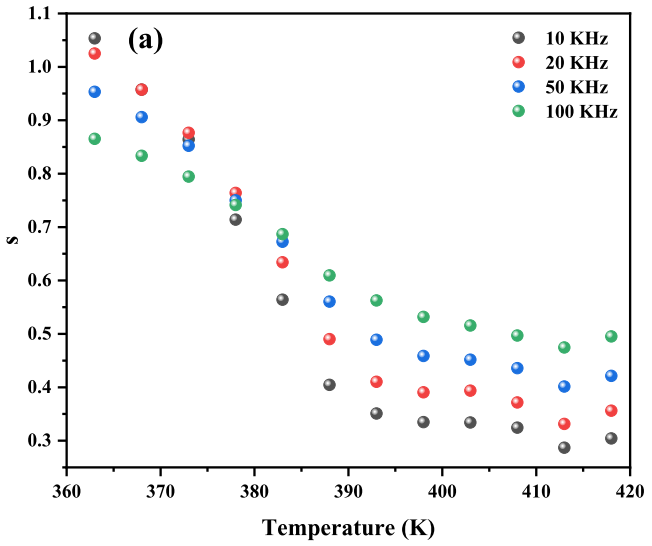

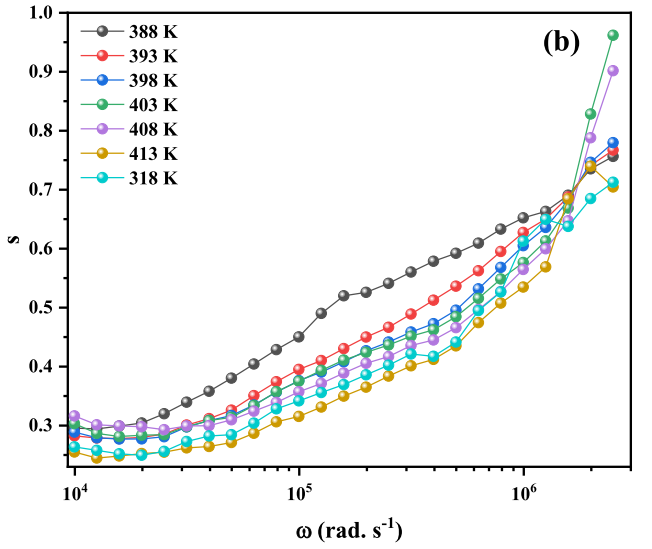

Figure 12. (a) Temperature and (b) frequency dependence of s in accordance with the CBH conduction mechanism.

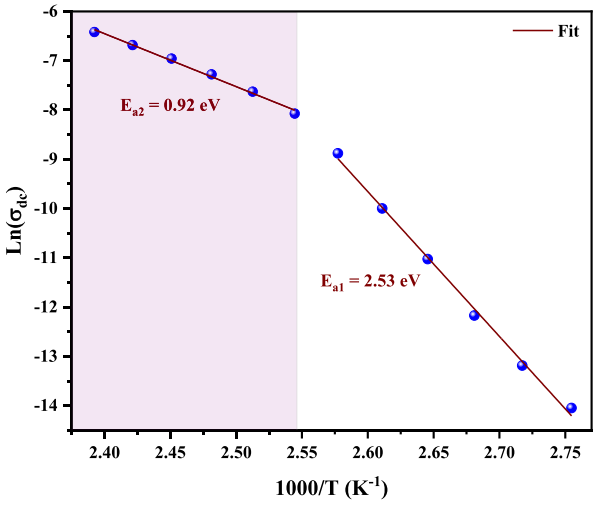

Figure 13. Reciprocal temperature dependence of σ_{dc}.

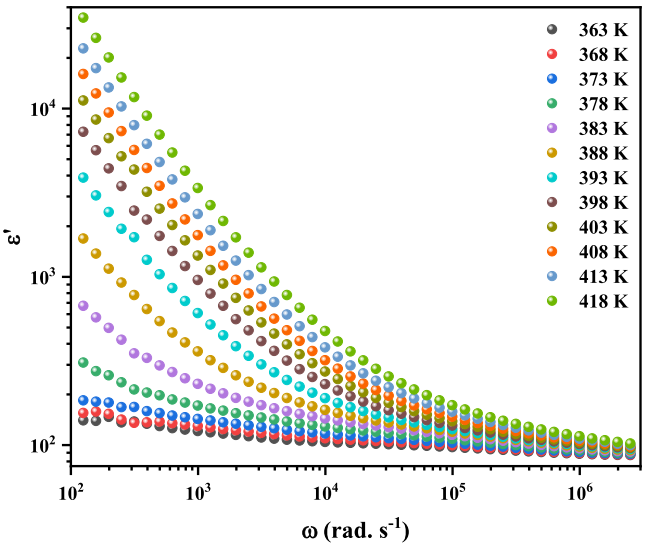

Figure 14. Frequency-dependent real part (ε') of the dielectric permittivity.

temperature does so at a particular frequency. This article describes how charge carriers are thermally activated, which affects polarization. Ionic, orientational, electronic, and interfacial polarization are the four primary categories of polarization. The orientational and interfacial polarizations of the system are relaxation components, whereas the electronic and ionic polarizations are deformational components of polarizability.[80] According to Koop's phenomenological theory, the fluctuation in ε' with frequency might be explained by Maxwell–Wagner interfacial polarization.[81] This model's material is anticipated to have conducted grains divided by ineffectively conducting grain borders. Therefore, charge carriers become stuck at the interface of grain boundaries to impede their passage.[81,82] The interfacial polarization process involves the exchange of electrons between ions that are part of the same molecules. Changes in the distribution and location of positive and negative space charges are caused by deformities and flaws in the material. Under the influence of the applied electric field, positive and negative charges, respectively, go toward the positive and negative poles of the applied electric field.[83] For our compound, we see that although electrons can hop to the grain boundary region in the low-frequency zone, they collect at the border and induce polarization due to the high grain boundary resistance. Nonetheless, electrons are unable to follow the high-frequency alternation of the applied field, even if they travel in the opposite direction, which stops them from continuing to accumulate electrons. It follows that the probability of electrons reaching the grain boundary reduces as the frequency increases and the polarization thins.[83] High frequency, on the other hand, does not significantly alter the value of ε'. The permittivity value that is "unrelaxed" demonstrates both atomic and electronic polarization.

In contrast, it was crucial to research the "dissipation factor," which is symbolized by tan(δ) in Figure 15, in materials for electronic applications. Where δ is the "loss angle", which is described mathematically as the angle formed by the voltage and charging current.[84] The dielectric loss was primarily caused by four physical processes: interfacial polarization, dielectric relaxation, conduction, and the molecule dipole moment.[85]

https://doi.org/10.1021/acsomega.4c01997
ACS Omega 2024, 9, 28339−28353

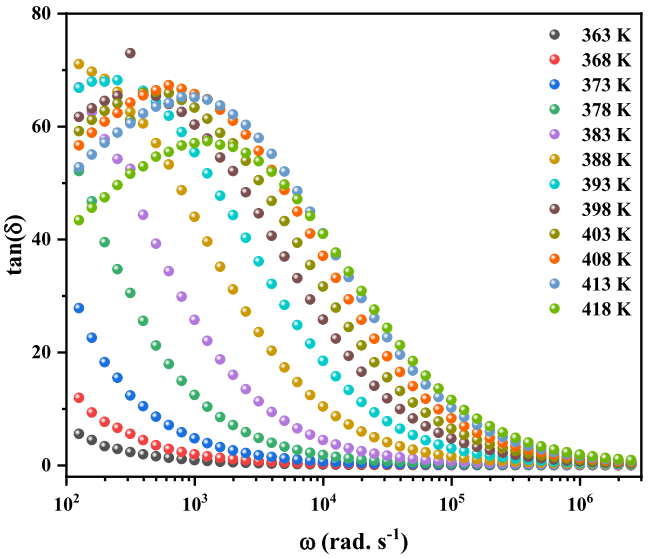

Figure 15. tan(δ) vs angular frequency spectra of $(C_{12}H_{17}N_2)_2[CdBr_4]$.

More energy is required to generate charge carrier mobility in the low-frequency range. As a result, tan(δ) values are higher for this frequency range.[86] As frequency increases, the material's resistivity lowers, requiring less energy to move charge carriers. As a result, the high-frequency region's dielectric loss decreases. This made it conceivable to think about employing these materials in electrical devices.[87]

The dielectric constant of a material is measured when it is exposed to an electric current to evaluate its capacity to store electrical energy. Higher dielectric constant values indicate a better charge storage capacity. Dielectric loss, on the other hand, measures the amount of energy lost as heat when a material is subjected to an alternating electric field. Lower dielectric loss values indicate a higher energy efficiency of the material, which is important in microelectronic applications where energy consumption must be minimized. As a result, the dielectric characteristics of this sample, which include a high dielectric constant and little dielectric loss at high frequencies, suggest that these materials may be effective in energy storage applications.

4. CONCLUSIONS

In conclusion, the $(C_{12}H_{17}N_2)_2[CdBr_4]$ compound was successfully created at room temperature by using the slow evaporation solution growth technique. The structural, optical, and overall electric properties were investigated. The absorption spectra have been computed using the theory of TD-DFT/B3LYP-D3/LanL2DZ. Therefore, there is a strong match between theoretical absorption and real spectra. The UV−visible spectral analysis reveals a band gap energy of 2.9 eV. This value demonstrates the suitability of the titular chemical for use in optoelectronic applications. The effects of the temperature on the relaxation and electronic transport processes in $(C_{12}H_{17}N_2)_2[CdBr_4]$ have been examined. Within the context of AC conductivity, the universal power law model was utilized to examine the frequency dependence of electric data. With a high dielectric constant ($\varepsilon \sim 10^5$) and negligible dielectric loss in the high-frequency range, this compound shows an attractive prospect for applications in energy storage.

ASSOCIATED CONTENT

Data Availability Statement

All data generated or analyzed during this study are available on reasonable request.

AUTHOR INFORMATION

Corresponding Author

Abderrazek Oueslati − *Laboratoire de Caractérisation Spectroscopique et Optique des Matériaux, Faculté des Sciences, Université de Sfax, 3000 Sfax, Tunisia;* orcid.org/0000-0002-3221-3401; Email: oueslatiabderrazek@yahoo.fr

Authors

Arafet Ghoudi − *Laboratoire de Caractérisation Spectroscopique et Optique des Matériaux, Faculté des Sciences, Université de Sfax, 3000 Sfax, Tunisia*

Sandy Auguste − *Institut des Molécules et Matériaux du Mans (IMMM), UMR-6283 CNRS, Le Mans Université, 72085 Le Mans Cedex 9, France*

Jérome Lhoste − *Institut des Molécules et Matériaux du Mans (IMMM), UMR-6283 CNRS, Le Mans Université, 72085 Le Mans Cedex 9, France;* orcid.org/0000-0002-4570-6459

Walid Rekik − *Laboratory Physical-Chemistry of Solid State, Chemistry Department, Faculty of Sciences of Sfax, University of Sfax, 3000 Sfax, Tunisia*

Houcine Ghalla − *Quantum and Statistical Physics Laboratory, Faculty of Sciences, University of Monastir, Monastir 5079, Tunisia*

Kamel Khirouni − *Laboratory of Physics of Materials and Nanomaterials Applied to the Environment (LaPHYMNE), Faculty of Sciences of Gabès cited Erriadh, 6079 Gabès, Tunisia*

Abdelhedi Aydi − *Laboratory of Multifunctional Materials and Applications (LaMMA), LR16ES18, Faculty of Sciences, University of Sfax, 3000 Sfax, Tunisia*

Complete contact information is available at: https://pubs.acs.org/10.1021/acsomega.4c01997

Funding

The authors declare that they have no known competing financial interests or personal relationships that could have appeared to influence the work reported in this paper.

Notes

The authors declare no competing financial interest.

ACKNOWLEDGMENTS

A great thanks to IMMM Mans France, especially the XR diffraction service.

REFERENCES

(1) Azouzi, K.; Hamdi, B.; Zouari, R.; Salah, A. B. Synthesis, structure and Hirshfeld surface analysis, vibrational and DFT investigation of (4-pyridine carboxylic acid) tetrachlorocuprate (II) monohydrate. *Bull. Mater. Sci.* **2017**, *40*, 289−299.

(2) Elgahami, H.; Trigui, W.; Oueslati, A.; Hlel, F. Structural, thermal analysis, and electrical conductivity of new organic-inorganic [(C4H9)4P]SbCl4 compound. *Ionics* **2019**, *25*, 1359−1371.

(3) Zhang, L.; Wang, J.; Wu, J.; Mo, S.; Long, F.; Zou, Z.; Gao, Y. Crystal structure, optical behavior and electrical conduction of the new organic−inorganic compound CH3NH3CdI3. *J. Mater. Sci: Mater. Electron* **2018**, *29*, 9821−9828.

https://doi.org/10.1021/acsomega.4c01997
ACS Omega 2024, 9, 28339−28353

(4) Ben Ahmed, A.; Feki, H.; Abid, Y. Synthesis, crystal structure, vibrational spectroscopy, optical properties and theoretical studies of a new organic−inorganic hybrid material: [((CH3)2NH2)+]6·[(BiBr6)3−]2. *Spectrochimica Acta Part A: Molecular and Biomolecular Spectroscopy* **2014**, *133*, 357−364.
(5) Liu, H.; Zhu, Q.; Feng, L.; Yao, B.; Feng, S. Synthesis, structural characterization and properties of a cubic octa-n-propylsilsesquioxane inorganic−organic hybrid material. *J. Mol. Struct.* **2013**, *1032*, 29−34.
(6) Ben Brahim, Kh.; Gzaiel, M. Ben; Oueslati, A.; Hlel, F.; Gargouri, M. Synthesis, structural characterization and electrical conduction mechanism of the new organic−inorganic complex: ([(C3H7)4N]FeCl4). *Mater. Res. Bull.* **2019**, *118*, No. 110505.
(7) Lefi, R.; Ben Nasr, F.; Hrichi, H.; Guermazi, H. Optical, electrical properties and characterization of (C2H5NH3)2CdCl4 compound. *Optik* **2016**, *127*, 5534−5541.
(8) Mao, W.; Wang, J.; Hu, X.; Zhou, B.; Zheng, G.; Mo, S.; Li, S.; Long, F.; Zou, Z. Synthesis, crystal structure, photoluminescence properties of organic-inorganic hybrid materials based on ethylenediamine bromide. *Journal of Saudi Chemical Society* **2020**, *24*, 52−60.
(9) Pardo, R.; Zayat, M.; Levy, D. Photochromic organic−inorganic hybrid materials. *Chem. Soc. Rev.* **2011**, *40*, 672−687.
(10) Zhou, C.; Yu, J.; Dong, H.; Yuan, F.; Zheng, X.; Jiang, M.; Zhang, L. Broad-band lead halide perovskite quantum dot single-mode lasers. *J. Mater. Chem. C* **2020**, *8*, 13642−13647.
(11) Tu, Y.; Xu, G.; Yang, X.; Zhang, Y.; Li, Z.; Su, R.; Luo, D.; Yang, W.; Miao, Y.; Cai, R.; Jiang, L.; Du, X.; Yanchu, Y.; Liu, Q.; Gao, Y.; Zhao, S.; Huang, W.; Gong, Q.; Zhu, R. Mixed-cation perovskite solar cells in space. *Sci. China: Phys., Mech. Astron.* **2019**, *62*, No. 974221.
(12) Vasilopoulou, M.; Kim, B. S.; Kim, H. P.; da Silva, W. J.; Schneider, F. K.; Mat Teridi, M. A.; Gao, P.; Abd, R.; Yusoff, Bin Mohd; Nazeeruddin, M. K. Perovskite Flash Memory with a Single-Layer Nanofloating Gate. *Nano Lett.* **2020**, *20*, 5081−5089.
(13) De Bastiani, M.; Saidaminov, M. I.; Dursun, I.; Sinatra, L.; Peng, W.; Buttner, U.; Mohammed, O. F.; Bakr, O. M. Thermochromic Perovskite Inks for Reversible Smart Window Applications. *Chem. Mater.* **2017**, *29*, 3367−3370.
(14) Tailor, N. K.; Kar, S.; Mishra, P.; These, A.; Kupfer, C.; Hu, H.; Awais, M.; Saidaminov, M.; Dar, M. I.; Brabec, C.; Satapathi, S. Advances in Lead-Free Perovskite Single Crystals: Fundamentals and Applications. *ACS Materials Lett.* **2021**, *3*, 1025−1080.
(15) Lian, Z.; Yan, Q.; Lv, Q.; Wang, Y.; Liu, L.; Zhang, L.; Pan, S.; Li, Q.; Wang, L.; Sun, J.-L. High-Performance Planar-Type Photodetector on (100) Facet of MAPbI3 Single Crystal. *Sci. Rep* **2015**, *5*, 16563.
(16) Liu, Y.; Zhang, Y.; Zhao, K.; Yang, Z.; Feng, J.; Zhang, X.; Wang, K.; Meng, L.; Ye, H.; Liu, M.; Liu, S. Frank A 1300 mm2 Ultrahigh-Performance Digital Imaging Assembly using High-Quality Perovskite Single Crystals. *Adv. Mater.* **2018**, *30*, No. 1707314.
(17) Karoui, K.; Hajlaoui, F.; Audebrand, N.; Roisnel, T.; Ben Rhaiem, A. Synthesis, crystal structures, high-temperatures phase transition, optic and electric properties of hybrid halogenometallates: [(CH3)3N(CH2)2Br]2[MIIBr4] (M = Cu, Zn). *J. Alloys Compd.* **2020**, *844*, No. 156115.
(18) Ben Bechir, M.; Karoui, K.; Tabellout, M.; Guidara, K.; Ben Rhaiem, A. Alternative current conduction mechanisms of organic-inorganic compound [N(CH3)3H]2CuCl4. *J. Appl. Phys.* **2014**, *115*, No. 203712.
(19) Elwej, R.; Hamdi, M.; Hannachi, N.; Hlel, F. Synthesis, structural characterization and dielectric properties of (C6H9N2)2-(Hg0.75Cd0.25)Cl4 compound. *Spectrochimica Acta Part A: Molecular and Biomolecular Spectroscopy* **2014**, *121*, 632−640.
(20) Chaabane, I.; Hlel, F.; Guidara, K. Synthesis, Infra-red, Raman, NMR and structural characterization by X-ray Diffraction of [C12H17N2]2CdCl4 and [C6H10N2]2Cd3Cl10compounds. *PMC Physics B* **2008**, *1*, 11.
(21) Jian, F. F.; Zhao, P. S.; Wang, Q. X.; Li, Y. One-dimensional Cd metal string complex: Synthesis, structural and thermal properties of [(HPy)3(Cd3Cl9)]∞. *Inorg. Chim. Acta* **2006**, *359*, 1473−1477.
(22) Corradi, A. B.; Cramarossa, M. R.; Saladini, M.; Battaglia, L. P.; Giusti, J. One-dimensional polymeric chlorocadmate(II) systems of N-methylpiperazinium and N,N′-dimethylpiperazinium compounds: synthesis, structural and thermal properties. *Inorg. Chim. Acta* **1995**, *230*, 59−65.
(23) Chaabane, I.; Hlel, F.; Guidara, K. Electrical study by impedance spectroscopy of the new compound [C12H17N2]2CdCl4. *J. Alloys Compd.* **2008**, *461*, 495−500.
(24) Selwin Joseyphus, R.; Viswanathan, E.; Justin Dhanaraj, C.; Joseph, J. Dielectric properties and conductivity studies of some tetradentate cobalt(II), nickel(II), and copper(II) Schiff base complexes. *Journal of King Saud University - Science* **2012**, *24*, 233−236.
(25) Bryndal, I.; Kucharska, E.; Sąsiadek, W.; Wandas, M.; Lis, T.; Lorenc, J.; Hanuza, J. Molecular and crystal structures, vibrational studies and quantum chemical calculations of 3 and 5-nitroderivatives of 2-amino-4-methylpyridine. *Spectrochimica Acta Part A: Molecular and Biomolecular Spectroscopy* **2012**, *96*, 952−962.
(26) Bruker, S.; Saint, S. *Bruker AXS Inc*; Madison: Wisconsin, USA, 2002.
(27) Sheldrick, G.M., SADABS. Bruker AXS Inc.: Madison, Wisconsin, USA, *Acta Crystallographica Section E Structure Reports Online ISSN* (2002) 1600−5368.
(28) Sheldrick, G. M. SHELXT − Integrated space-group and crystal-structure determination. *Acta Cryst. A* **2015**, *71*, 3−8.
(29) Farrugia, L. J. WinGX suite for small-molecule single-crystal crystallography. *J. Appl. Crystallogr.* **1999**, *32*, 837−838.
(30) Sheldrick, G. M. Crystal structure refinement with SHELXL. *Acta Cryst. C* **2015**, *71*, 3−8.
(31) Brandenburg, K.; Putz, H. *Crystal Impact GbR*; Bonn, Germany, 2012, This Article Is Licensed under a Creative Commons Attribution 3 (n.d.).
(32) Yang, L.; Powell, D. R.; Houser, R. P. Structural variation in copper(I) complexes with pyridylmethylamide ligands: structural analysis with a new four-coordinate geometry index, τ4. *Dalton Trans* **2007**, 955−964.
(33) Msalmi, R.; Elleuch, S.; Hamdi, B.; Zouari, R.; Naïli, H. Synthesis, DFT calculations, intermolecular interactions and third order nonlinear optical properties of new organoammonium tetrabromocadmate (II): (C5H6N2Cl)2[CdBr4]·H2O. *J. Mol. Struct.* **2020**, *1222*, No. 128853.
(34) Sharma, R. P.; Sharma, R.; Bala, R.; Salas, J. M.; Quiros, M. , Second sphere coordination complexes via hydrogen bonding: Synthesis, spectroscopic characterisation of [trans-Co(en)2Cl2]CdX4 (X = Br or I) and single crystal X-ray structure determination of [trans-Co(en)2Cl2]CdBr4. *J. Mol. Struct.* **2006**, *794*, 341−347.
(35) Altermatt, D.; Arend, H.; Niggli, A.; Petter, W. New tetrahedrally coordinated A2CdBr4 compounds (A = Cs, CH3NH3). *Mater. Res. Bull.* **1979**, *14*, 1391−1396.
(36) Baur, W. H. The geometry of polyhedral distortions Predictive relationships for the phosphate group. *Acta Cryst. B* **1974**, *30*, 1195−1215.
(37) Sinnokrot, M. O.; Valeev, E. F.; Sherrill, C. D. Estimates of the Ab Initio Limit for π−π Interactions: The Benzene Dimer. *J. Am. Chem. Soc.* **2002**, *124*, 10887−10893.
(38) Khan, S. A.; Al-Hazmi, F. S.; Al-Heniti, S.; Faidah, A. S.; Al-Ghamdi, A. A. Effect of cadmium addition on the optical constants of thermally evaporated amorphous Se−S−Cd thin films. *Curr. Appl. Phys.* **2010**, *10*, 145−152.
(39) Lv, J.; Xu, M.; Lin, S.; Shao, X.; Zhang, X.; Liu, Y.; Wang, Y.; Chen, Z.; Ma, Y. Direct-gap semiconducting tri-layer silicene with 29% photovoltaic efficiency. *Nano Energy* **2018**, *51*, 489−495.
(40) Kobayashi, N.; Kuwae, H.; Oshima, J.; Ishimatsu, R.; Tashiro, S.; Imato, T.; Adachi, C.; Shoji, S.; Mizuno, J. A wide-energy-gap naphthalene-based liquid organic semiconductor host for liquid deep-blue organic light-emitting diodes. *J. Lumin.* **2018**, *200*, 19−23.
(41) Kalthoum, R.; Ben Bechir, M.; Ben Rhaiem, A. CH3NH3CdCl3: A promising new lead-free hybrid organic−

https://doi.org/10.1021/acsomega.4c01997
ACS Omega 2024, 9, 28339−28353

inorganic perovskite for photovoltaic applications. *Physica E: Low-Dimensional Systems and Nanostructures* **2020**, *124*, No. 114235.
(42) Qaid, S. M. H.; Al-Asbahi, B. A.; Ghaithan, H. M.; AlSalhi, M. S.; Al Dwayyan, A. S. Optical and structural properties of CsPbBr3 perovskite quantum dots/PFO polymer composite thin films. *J. Colloid Interface Sci.* **2020**, *563*, 426−434.
(43) Tauc, J. *Amorphous and Liquid Semiconductors*; Springer Science & Business Media, 2012.
(44) Gagandeep, K.; Singh, B. S.; Lark, H. S. Sahota, Attenuation Measurements in Solutions of Some Carbohydrates. *Nucl. Sci. Eng.* **2000**, *134*, 208−217.
(45) Kammoun, I.; Belhouchet, M.; Ahmed, A. B.; Lhoste, J.; Gargouri, M. Investigation of structural, optical and electrical conductivity of a new organic inorganic bromide: [C 12 H 17 N 2] 2 ZnBr 4. *RSC Adv.* **2023**, *13*, 8034−8042.
(46) Shahane, G. S.; More, B. M.; Rotti, C. B.; Deshmukh, L. P. Studies on chemically deposited CdS1−xSex mixed thin films. *Mater. Chem. Phys.* **1997**, *47*, 263−267.
(47) Bhattacharyya, D.; Chaudhuri, S.; Pal, A. Bandgap and optical transitions in thin films from reflectance measurements. *Vacuum* **1992**, *43*, 313−316.
(48) Runge, E.; Gross, E. K. U. Density-Functional Theory for Time-Dependent Systems. *Phys. Rev. Lett.* **1984**, *52*, 997−1000.
(49) *R.A. Gaussian09, 1*, Frisch, Mj, Trucks, Gw, Schlegel, Hb, Scuseria, Ge, Robb, Ma, Cheeseman, Jr, Scalmani, G.; Barone, V.; Mennucci, B.; Petersson, Ga et al., Gaussian, Inc.: Wallingford CT, *121* (2009) 150−166.
(50) Kim, K.; Jordan, K. D. Comparison of Density Functional and MP2 Calculations on the Water Monomer and Dimer. *J. Phys. Chem.* **1994**, *98*, 10089−10094.
(51) Grimme, S. Semiempirical hybrid density functional with perturbative second-order correlation. *J. Chem. Phys.* **2006**, *124*, No. 034108.
(52) Grimme, S.; Antony, J.; Ehrlich, S.; Krieg, H. A consistent and accurate ab initio parametrization of density functional dispersion correction (DFT-D) for the 94 elements H-Pu. *J. Chem. Phys.* **2010**, *132*, 154104.
(53) Mhadhbi, N.; Saïd, S.; Elleuch, S.; Naïli, H. Crystal structure, spectroscopy, DFT studies and thermal characterization of Cobalt(II) complex with 2-protonated aminopyridinium cation as ligand. *J. Mol. Struct.* **2016**, *1108*, 223−234.
(54) Ebrahimipour, S. Y.; Khosravan, M.; White, J.; Fekri, S. Preparation, crystal structure, spectroscopic studies, DFT calculations, antibacterial activities and molecular docking of a tridentate Schiff base ligand and its cis-MoO2 complex. *Appl. Organomet. Chem.* **2018**, *32*, No. e4233.
(55) Dang, Y.; Zhong, C.; Zhang, G.; Ju, D.; Wang, L.; Xia, S.; Xia, H.; Tao, X. Crystallographic Investigations into Properties of Acentric Hybrid Perovskite Single Crystals NH(CH3)3SnX3 (X = Cl, Br). *Chem. Mater.* **2016**, *28*, 6968−6974.
(56) Bouokkeze, D.; Massoudi, J.; Hzez, W.; Smari, M.; Bougoffa, A.; Khirouni, K.; Dhahri, E.; Bessais, L. Investigation of the structural, optical, elastic and electrical properties of spinel LiZn 2 Fe 3 O 8 nanoparticles annealed at two distinct temperatures. *RSC Adv.* **2019**, *9*, 40940−40955.
(57) Mesrar, M.; Lamcharfi, T.; Echatoui, N.-S.; Abdi, F. Effect of sintering temperature on the microstructure and electrical properties of (Na0.5Bi0.5)TiO3 processed by the sol-gel method. *J. Sol-Gel Sci. Technol.* **2022**, *103*, 820−831.
(58) Pal, P.; Ghosh, A. Robust Succinonitrile Plastic Crystal-Based Ionogel for All-Solid-State Li-Ion and Dual-Ion Batteries. *ACS Appl. Energy Mater.* **2020**, *3*, 4295−4304.
(59) Bechir, M. B.; Houcine Dhaou, M. Study of charge transfer mechanism and dielectric relaxation of all-inorganic perovskite CsSnCl3. *RSC Adv.* **2021**, *11*, 21767−21780.
(60) Schmidt, R.; Brinkman, A. W. Studies of the Temperature and Frequency Dependent Impedance of an Electroceramic Functional Oxide NTC Thermistor. *Adv. Funct. Mater.* **2007**, *17*, 3170−3174.
(61) Javed, M.; Arif Khan, A.; Kazmi, J.; Akbar, N.; Ahmed, N.; Khisro, S. N.; Mohamed, M. A. Investigation on electrical transport and dielectric relaxation mechanism in TbCrO3 perovskite orthochromite. *J. Alloys Compd.* **2023**, *955*, No. 170181.
(62) Moulahi, A.; Guesmi, O.; Abdelbaky, M. S. M.; García-Granda, S.; Dammak, M. Structural characterization, thermal analysis, electric and dielectric properties of a novel organic-inorganic hybrid compound based on iron fluoride. *J. Alloys Compd.* **2022**, *898*, No. 162956.
(63) Lu, X.; Dong, C.; Guo, X.; Ren, J.; Xue, H.; Tang, F.; Ding, Y. Effects of grain size and temperature on mechanical properties of nano-polycrystalline Nickel-cobalt alloy. *Journal of Materials Research and Technology* **2020**, *9*, 13161−13173.
(64) Rahmouni, H.; Smari, M.; Cherif, B.; Dhahri, E.; Khirouni, K. Conduction mechanism, impedance spectroscopic investigation and dielectric behavior of La0.5Ca0.5−xAgxMnO3 manganites with compositions below the concentration limit of silver solubility in perovskites ($0 \leq x \leq 0.2$). *Dalton Trans.* **2015**, *44*, 10457−10466.
(65) Pattanayak, D. K.; Parida, R. K.; Nayak, N. C.; Panda, A. B.; Parida, B. N. Optical and transport properties of new double perovskite oxide. *J. Mater. Sci: Mater. Electron* **2018**, *29*, 6215−6224.
(66) Pradhan, D. K.; Misra, P.; Puli, V. S.; Sahoo, S.; Pradhan, D. K.; Katiyar, R. S. Studies on structural, dielectric, and transport properties of Ni0.65Zn0.35Fe2O4. *J. Appl. Phys.* **2014**, *115*, 243904.
(67) Ray, A.; Roy, A.; De, S.; Chatterjee, S.; Das, S. Frequency and temperature dependent dielectric properties of TiO2-V2O5 nano-composites. *J. Appl. Phys.* **2018**, *123*, 104102.
(68) Starczewska, A.; Toroń, B.; Szperlich, P.; Nowak, M. Electrical Property Analysis of Textured Ferroelectric Polycrystalline Antimony Sulfoiodide Using Complex Impedance Spectroscopy. *Materials* **2021**, *14*, 2579.
(69) Ghoudi, A.; Brahim, K.; Ghalla, H.; Lhoste, J.; Auguste, S.; Khirouni, K.; Abdelhedi, A.; Oueslati, A. Crystal structure and optical characterization of a new hybrid compound, C 6 H 9 N 2 FeCl 4, with large dielectric constants for field-effect transistors †. *RSC Adv.* **2023**, *13*, 12844−12862.
(70) Das, P. R.; Parida, B. N.; Padhee, R.; Choudhary, R. N. P. Electrical properties of Na2Pb2R2W2Ti4V4O30 (R = Dy, Pr) ceramics. *J. Adv. Ceram* **2013**, *2*, 112−118.
(71) Ghosh, A.; Chakravorty, D. AC conduction in semiconducting CuO-Bi2O3-P2O5 glasses. *J. Phys.: Condens. Matter* **1990**, *2*, 5365.
(72) Cleach, X. L. Lois de variations et ordre de grandeur de la conductivité alternative des chalcogénures massifs non cristallins. *J. Phys. (Paris)* **1979**, *40*, 417−428.
(73) Pike, G. E. ac Conductivity of Scandium Oxide and a New Hopping Model for Conductivity. *Phys. Rev. B* **1972**, *6*, 1572−1580.
(74) Elliott, S. R. Temperature dependence of a.c. conductivity of chalcogenide glasses. *Philosophical Magazine B* **1978**, *37*, 553−560.
(75) Nowick, A. S.; Lim, B. S.; Vaysleyb, A. V. Nature of the ac conductivity of ionically conducting crystals and glasses. *J. Non-Cryst. Solids* **1994**, *172−174*, 1243−1251.
(76) Lee, W. K.; Liu, J. F.; Nowick, A. S. Limiting behavior of ac conductivity in ionically conducting crystals and glasses: A new universality. *Phys. Rev. Lett.* **1991**, *67*, 1559−1561.
(77) Tammam, A. K.; Gawad, D.; Mostafa, M. F. Crossover from overlap large polaron to small polaron tunneling: A study of conduction mechanisms and phase transitions in a new long chain organic inorganic hybrid. *J. Phys. Chem. Solids* **2021**, *149*, No. 109787.
(78) Weir, W. B. Automatic measurement of complex dielectric constant and permeability at microwave frequencies. *Proceedings of the IEEE* **1974**, *62*, 33−36.
(79) Dabbebi, T.; Hcini, S.; Alzahrani, B.; Rahmouni, H.; Dhahri, E.; Al Robei, H.; Bouazizi, M. L. Structural and dielectric behaviors for Mg0.5Co0.5Fe2O4 spinel ferrite synthesized by sol−gel route. *J. Mater. Sci: Mater. Electron* **2022**, *33*, 490−504.
(80) Sahoo, A.; Paul, T.; Maiti, S.; Banerjee, R. Temperature-dependent dielectric properties of CsPb2Br5: a 2D inorganic halide perovskite. *Nanotechnology* **2022**, *33*, 195703.

https://doi.org/10.1021/acsomega.4c01997
ACS Omega 2024, 9, 28339−28353

(81) Koops, C. G. On the Dispersion of Resistivity and Dielectric Constant of Some Semiconductors at Audiofrequencies. *Phys. Rev.* **1951**, *83*, 121−124.
(82) Ahmad, M.; Rafiq, M. A.; Rasool, K.; Imran, Z.; Hasan, M. M. Dielectric and transport properties of bismuth sulfide prepared by solid state reaction method. *J. Appl. Phys.* **2013**, *113*, No. 043704.
(83) Thongbai, P.; Tangwancharoen, S.; Yamwong, T.; Maensiri, S. Dielectric relaxation and dielectric response mechanism in (Li, Ti)-doped NiO ceramics. *J. Phys.: Condens. Matter* **2008**, *20*, No. 395227.
(84) Bhuyan, P.; Cho, D.; Choe, M.; Lee, S.; Park, S. Liquid Metal Patterned Stretchable and Soft Capacitive Sensor with Enhanced Dielectric Property Enabled by Graphite Nanofiber Fillers. *Polymers* **2022**, *14*, 710.
(85) Kao, K.C.; *Electric Polarization and Relaxation in Dielectric Phenomena in Solids*, 2004.
(86) Gaâbel, F.; Khlifi, M.; Hamdaoui, N.; Beji, L.; Taibi, K.; Dhahri, J. Microstructural, structural and dielectric analysis of Ni-doped CaCu3Ti4O12 ceramic with low dielectric loss. *J. Mater. Sci: Mater. Electron* **2019**, *30*, 14823−14833.
(87) Singh, S.; Banappanavar, G.; Kabra, D. Correlation between Charge Transport Length Scales and Dielectric Relaxation Time Constant in Hybrid Halide Perovskite Semiconductors. *ACS Energy Lett.* **2020**, *5*, 728−735.

https://doi.org/10.1021/acsomega.4c01997
ACS Omega 2024, 9, 28339−28353